Failure of cemented granular materials under simple compression - Experiments and numerical simulations

Jean-Yves Delenne, Vincent Topin, Farhang Radjai

Failure of cemented granular materials under simple compression – Experiments and numerical simulations

J.-Y. Delenne[a,b], V. Topin[a,c] and F. Radjai[a,b]
[a] LMGC, UMR 5508 CNRS–UM2, Cc 048, 34095 Montpellier cedex 5, France
[b] MIST, IRSN CNRS–DPAM, Cc 048, 34095 Montpellier cedex 5, France
[c] IATE, CNRS–INRA, 2 place Pierre Viala, 34060 Montpellier cedex 1, France
corresponding author: delenne@lmgc.univ-montp2.fr

2009

Abstract

We investigate the strength and failure properties of a model cemented granular material under simple compressive deformation. The particles are LECA beads coated by a controlled volume fraction of silicone. The beads are mixed with a joint seal paste (the matrix) and moulded to obtain dense cemented granular samples of cylindrical shape. Several samples are prepared for different volume fractions of the matrix, controlling the porosity, and silicone coating upon which depends the effective particle-matrix adhesion. Interestingly, the compressive strength is found to be an affine function of the product of the matrix volume fraction and effective particle-matrix adhesion. On the other hand, it is shown that particle damage occurs beyond a critical value of the contact debonding energy. The experiments suggest three regimes of crack propagation corresponding to no particle damage, particle abrasion and particle fragmentation, respectively, depending on the matrix volume fraction and effective particle-matrix adhesion. We also use a sub-particle lattice discretization method to simulate cemented granular materials in 2D. The numerical results for crack regimes and the compressive strength are in excellent agreement with the experiments.
keywords: Granular materials Cementation Adhesion Compressive strength Toughness Lattice Element Method

1 Introduction

Cemented granular materials consist of densely packed particles and a solid matrix filling partially the interstitial space and sticking to the particles.

Well-known examples of this class of materials are mortars, concrete, asphalt, grouted soils and sedimentary rocks (sandstones, conglomerates and breccia) [18, 27, 5, 1, 31]. Experiments and numerical simulations indicate that the adherence between the particles and matrix controls to a large extent the toughness and crack patterns of cemented granular materials [27, 40, 18, 29, 30, 32]. However, due to the bulk action of the matrix, these materials are more complex than cohesive granular media with surface adhesion such as fine powders [16, 15, 23, 3, 8, 9]. In particular, the mechanical behavior (stiffness, tensile strength and creep resistance) depends on load transfer between the matrix and the particles [10, 28, 39].

The high volume fraction of the particles in cemented granular materials leads to a microstructure dominated by a network of contacting particles (jamming) as in cohesionless granular media [12, 22, 35, 23]. In this respect, cemented granular materials differ from dilute particle-reinforced composites where the particles are interposed by the matrix. The contact network has profound effect on stress transmission and local failure modes involving particle breakage, frictional slip and rolling [14, 10, 17, 7, 9, 8]. In particular, the arching effect leads to weakly stressed zones in the bulk, and the onset and propagation of fracture is mostly controlled by granular disorder [27]. For this reason, the models developed for dilute particle-reinforced materials cannot be simply extended to cemented granular materials [29].

Another specificity of cemented granular materials is that, as a result of steric effects, the interstitial space is generally only partially filled by the cementing matrix. As a result, these materials generally involve unfilled pores and micro-cleavages (particle-particle contacts not interposed by matrix) between particles. For example, there is experimental evidence that the interparticle contacts in grouted sand are not all cemented, leading to frictional behavior as in cohesionless granular media [1].

In this paper, we report on original experiments which were designed to investigate the influence of matrix volume fraction and particle-matrix-adhesion on the compressive strength and particle damage of cemented granular materials. We use a model system in which the particles are LECA (Lightweight Expanded Clay Aggregate) beads which can break under moderate load, and the matrix is a joint seal paste. The particle-matrix adhesion is controlled by coating the particles with the desired amount of silicone. We analyze the experimental data by considering the peak stress and particle damage under simple compression tests. The experimental results are compared with 2D numerical simulations by means of a lattice-element method in which the particles, matrix and their interface are discretized by linear elastic lattice elements with a breaking threshold [25, 27, 37].

In the following, we first introduce the experimental procedures in section 2. The experimental data will be analyzed and discussed in section 3. The numerical model is briefly introduced in section 4, and followed by the presentation of numerical results. Finally, in section 5, we conclude with a

summary and remarks about potential perspectives of this work.

2 Sample preparation and experimental protocol

The main objective of these experiments is to investigate the compressive strength of model granular materials in the presence of a cementing matrix. The choice of the materials and methods employed in these experiments was dictated by the following considerations: 1) The possibility of particle failure during deformation, 2) The variation of the volume fraction of the cementing matrix, and 3) The control of the adhesion at the particle-matrix interface. The compressive strength and failure modes of a cemented granular material depend on a combination of the above factors. Clearly, varying all these parameters in a systematic manner is a difficult task from an experimental viewpoint.

For the particles, we used the so-called "Lightweight expanded clay aggregate" (LECA) beads (also known as "fired clay pebble"). The LECA beads are porous and light with a rough surface and a weak variability in sphericity. The compressive strength of the beads is around 3.3 MPa, so that they can break under moderate compressive loads. The beads are first visually sorted in order to remove the damaged particles. The particle diameters d_g range from 8.0 mm to 16.0 mm and almost normally distributed. The mean diameter is 11.9 ± 0.3 mm.

As cementing matrix we used a commercial paste employed as joint seal for floor tiles. The LECA beads are mixed with the desired amount of paste in a box at ambient temperature and carefully stirred manually until a homogeneous mixture is obtained. This mixture is placed in a cylindrical mould (of height 190mm and diameter 94mm) whose internal wall is covered by a polyester film which has a weak adhesion with the cementing paste. The mixture is compacted layer by layer in order to obtain a dense packing, which is then unmoulded with its protective film.

At this stage, the samples are particularly delicate to handle since their cohesion is low. Hence, particular experimental precautions were necessary in order to avoid damage to the samples. In particular, the drying of the samples is performed in four steps: 1) Drying during one week at constant ambient temperature of 22^oC; 2) Removing the polyester film and drying one more week at the same temperature; 3) Drying three more weeks in a heat chamber at the temperature of 45^oC; and 4) Thermalizing the sample for one day at the ambient temperature before the compression test. This progressive process preserves the cohesive links both at the surface and within the samples and allows for uniform drying of the whole sample.

The adhesion of the matrix (paste) to the LECA beads is normally higher than the internal tensile strength of LECA beads. In order to reduce the interface adherence, we coated the LECA beads by an acetic-silicone glue

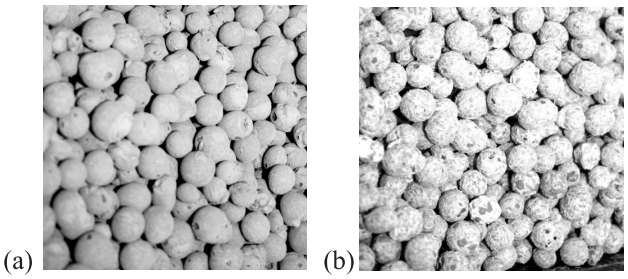

Figure 1: (a) LECA beads ; (b) LECA beads with silicone coating.

before mixing with the paste. The dried silicone has the property of sticking strongly to the rough surface of LECA beads while bearing a negligible adherence with the matrix. The effective adhesion between the matrix and the beads depends on the thickness of silicone coating. The latter was varied by mixing the beads with different volume fractions ρ^s of silicone. The quality of coating was controlled by visual inspection. We stop stirring when the beads show a slightly white-colored surface texture. The coated particles are left to dry for two days. Fig. 1 shows pictures of LECA beads without and with silicone coating before moulding.

Twenty cylindrical samples were prepared with five values of the matrix volume fraction $\rho^m = 0.10$, 0.15, 0.20, 0.25 and 0.30, each for four different values of the silicone volume fraction ρ^s =0.000, 0.008, 0.017, 0,033. The volume fraction of LECA beads is $\rho^p = 58 \pm 2\%$ for all samples. This number of samples is a necessary minimum to appreciate the qualitative behavior as a function of matrix volume fraction and the particle-matrix adhesion (controlled by the silicone volume fraction).

The uniaxial press used to perform compression tests on the samples is shown in Fig. 2. The downward displacement is imposed on the top plate with a rate of 0.05 mm s^{-1}. To avoid bending effects due to the defects in parallelism between the top and bottom surfaces of the sample, we used a pin joint. The loading force is recorded via a 25 kN load sensor. In each test, the compression is continued till full failure of the sample occurs.

In the following, we present and discuss our main experimental results by focussing on the compressive yield strength as a function of matrix volume fraction and the particle-matrix adhesion, as well as the corresponding failure modes.

3 Experimental results

Figure 3a shows the axial stress σ as a function of the axial deformation ε for two different values of the matrix volume fraction ρ^m. Both the initial axial stiffness E and peak stress σ_Y increase with ρ^m. Fig 3b shows similar

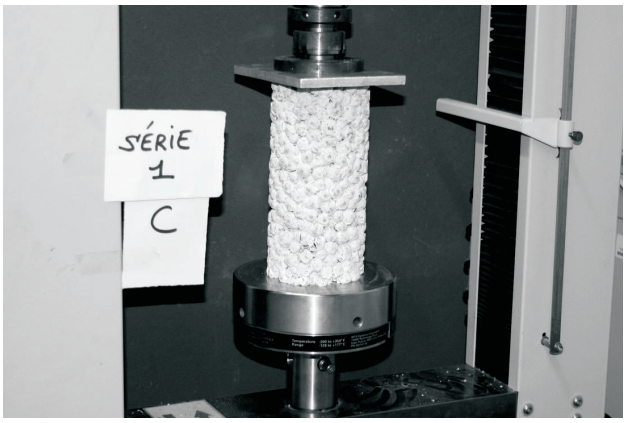

Figure 2: An experimental sample of cylindrical shape subjected to simple compression test.

plots for two different values of the silicone volume fraction ρ^s. We see that E and σ_Y decrease considerably with ρ^s.

The parameters ρ^m and ρ^s play also an important role in failure modes three examples of which are shown in Fig 3. Fig 3a is an example for a high value of ρ^m and a low value of ρ^s (weak particle-matrix interface). We observe a marked "barreling" failure occurring often in triaxial testing of soil specimen. Fig 3b corresponds to low values of ρ^m and ρ^s (strong particle-matrix interface). In this case, the rupture surface takes a conical shape. Fig 3c corresponds to high values of both ρ^m and ρ^s. The failure is brittle and localized on a plane.

Silicone deposit affects mainly the surface of the particles and thus the particle-matrix adhesion. The weakening of the interface depends on the thickness of silicone coating. Let σ^{sm} be the silicone-matrix interface adhesion and η the surface fraction of LECA beads coated by the silicone. The effective particle-matrix adhesion σ^{pm*} can be evaluated as a surface weighted mean of σ^{sm} and σ^{pm}:

$$\sigma^{pm*} = \eta\sigma^{sm} + (1-\eta)\sigma^{pm} \tag{1}$$

The coating fraction η depends on the roughness of the bead surface. The silicone paste covers an increasing fraction of asperity peaks as a function of the silicone volume V^s. The flow of silicone from peaks to hollows during the drying process can be neglected due to its high viscosity. The hollows are fully covered ($\eta = 1$) for a volume V^s_{sat} of silicone depending on the surface roughness.

Let us assume that there are N spherical asperities of the same radius R and different heights at the surface of each bead. Then, the total accessible surface S_{sat} is given by

$$S_{sat} = 2\pi R^2 N \tag{2}$$

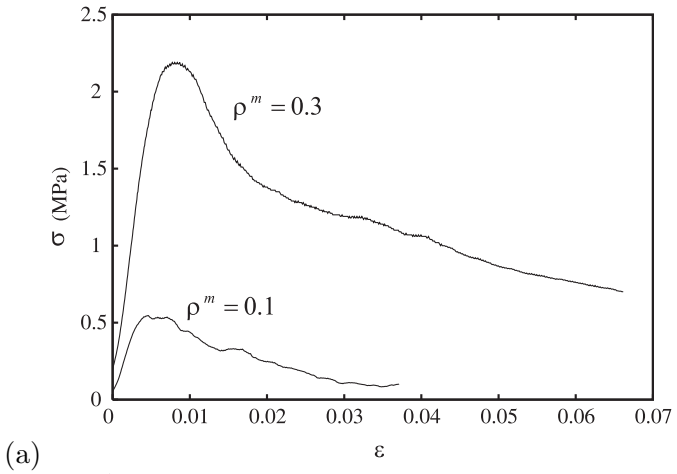

(a)

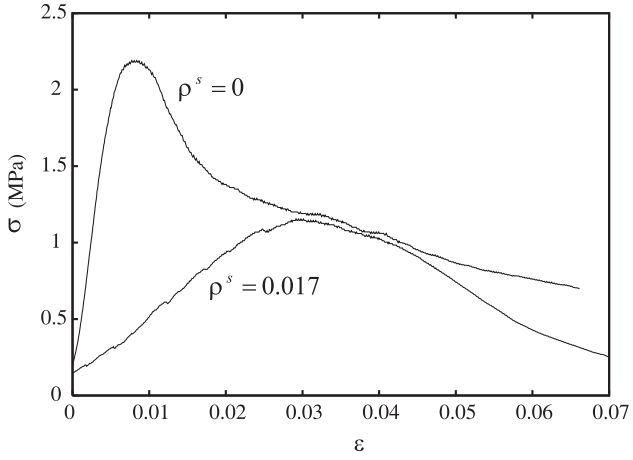

(b)

Figure 3: Examples of stress-strain plots: (a) Effect of the matrix volume fraction ρ^m; (b) Effect of the silicone volume fraction ρ^s.

(a) 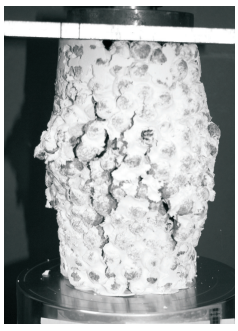 (b) 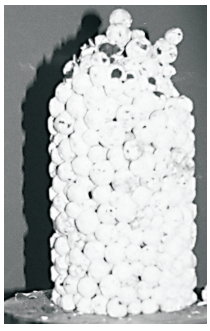 (c) 

Figure 4: Failure modes for high matrix volume fraction and strong particle-matrix adhesion (a), low matrix volume fraction and strong particle-matrix adhesion (b) and high matrix volume fraction and weak particle-matrix adhesion (c).

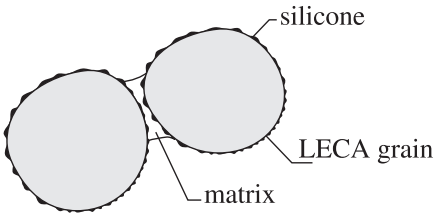

Figure 5: A schematic representation of the local geometry.

If all asperities are coated with a mean thickness δ, we have

$$V^s_{sat} = \delta S_{sat} = 2\pi R^2 N \delta \tag{3}$$

As a result, the mean coating fraction η is simply given by

$$\eta = \frac{V^s/\delta}{S_{sat}} = \frac{V^s}{V^s_{sat}} = \frac{\rho^s}{\rho^s_{sat}} \tag{4}$$

and we have

$$\sigma^{pm*} = \frac{\rho^s}{\rho^s_{sat}}\sigma^{sm} + (1 - \frac{\rho^s}{\rho^s_{sat}})\sigma^{pm} \tag{5}$$

Equation 5 can be improved by taking into account the statistics of roughness asperities. However, this information is not available for our LECA beads, and thus we will rely on equation 5 to express the effective particle-matrix adhesion in the presence of silicone coating from experimental values of the silicone volume fraction ρ^s. In this form, we need only the value of ρ^s_{sat} which depends on the surface roughness but can be determined from experiments. We have $\rho^s_{sat} \simeq 0.04$ and $\sigma^{sm} \ll \sigma^{pm}$, so that

$$\sigma^{pm*} \simeq \left(1 - \frac{\rho^s}{0.04}\right)\sigma^{pm} \tag{6}$$

Figure 6 shows the compressive strength (peak stress) σ_Y as a function of the matrix volume fraction ρ^m for different values of σ^{pm*}. The data are well fit by straight lines passing through the origin with an increasing slope as σ^{pm*} increases. The role of the matrix is two-fold. On one hand, the load transfer between the particles and matrix leads to higher homogeneity of stress transmission as ρ^m increases as a result of the reduction of porosity. On the other hand, the area S^{pm} of the matrix-particle interface, and thus the particle-matrix tensile force threshold $F^{pm} = \sigma^{pm*}\ S^{pm}$, increases with ρ^m. Let us assume that the matrix is distributed in the form of independent solid bonds between neighboring particles of an average gap e (see Fig. 5). With this assumption, and neglecting the effect of curvature at the interface, we have $S^{pm} \propto \rho^m$, and thus

$$F^{pm} \propto \sigma^{pm*}\ \rho^m. \tag{7}$$

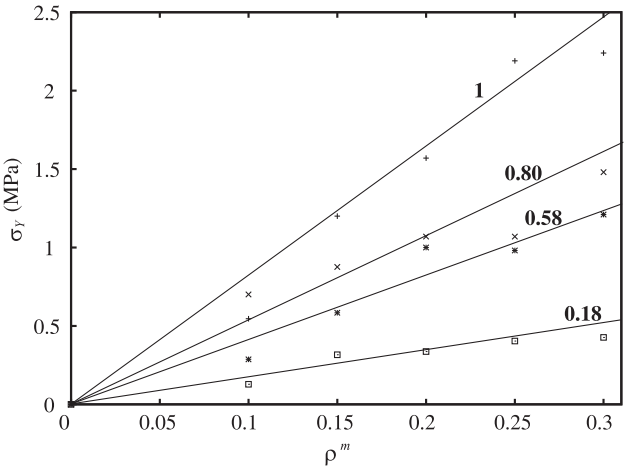

Figure 6: Compressive strength σ_Y as a function of the matrix volume fraction ρ^m for different values of particle-matrix adhesion σ^{pm*} normalized by the particle tensile strength σ^p.

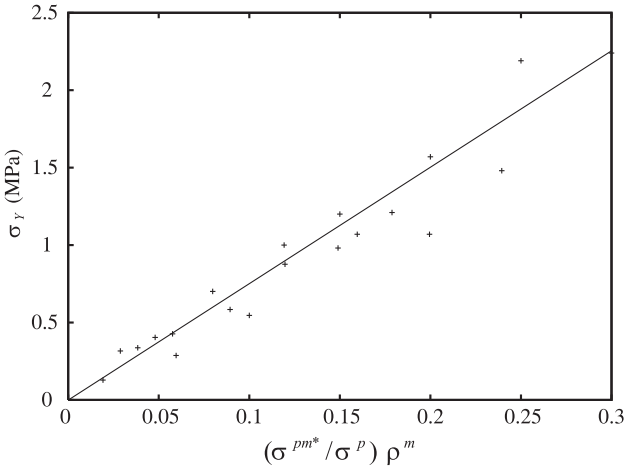

Figure 7: Compressive strength vs. the product $\sigma^{pm*}\ \rho^m$ fitted by a solid straight line passing through the origin.

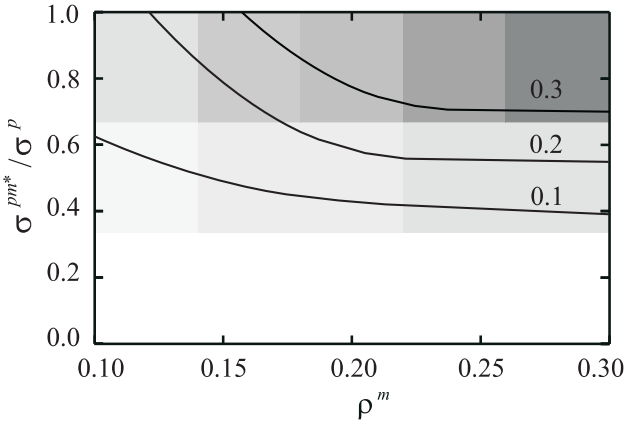

Figure 8: Grey-level map of the fraction of damaged particles as a function of the matrix volume fraction and particle-matrix adhesion.

We expect the effective tensile strength σ_Y to scale with the contact tensile force threshold F^{pm} and thus with the product σ^{pm*} ρ^m [9, 24]. In Fig. 7, σ_Y is plotted versus $\sigma^{pm*}\rho^m$ for all our compression tests. Interestingly, all data points collapse approximately on a straight line passing through the origin. This is a surprising result as the nonlinear curvature effects related to the spherical form of the particles can be neglected only at low values of ρ^m. At larger values, the matrix-particle interface area does not increase in proportion to matrix volume fraction. At very high values of ρ^m (above $\simeq 20\%$) the matrix percolates throughout the packing and the assumption of isolated solid bonds between the particles does not hold neither. The fact that the linear scaling holds even at large values of ρ^m may be attributed to the bulk effect of the matrix. Indeed, when the matrix percolates throughout the system, the interface area does not evolve with ρ^m whereas the load transfer between the particles and matrix is reinforced due to the possibility of stress transmission through the matrix.

An important aspect of the rupture of cemented granular materials is the amount of particle damage which reflects the composition of the material and the relative strengths of the constituents [18, 36, 20, 34, 30]. In the experiments, we are able to evaluate the number of damaged particles at the end of each test. This is done visually by counting the damaged particles in the fractured zones of the samples. Fig. 8 shows a gray-level map of the fraction of damaged particles in the parameter space (ρ^m,σ^{pm*}). A limit line can be distinguished below which no particle damage occurs. This regime is mainly controlled by σ^{pm*} for $\rho^m > 0.2$ whereas in the range $\rho^m < 0.2$ both parameters are important. Beyond this particle-damage limit, the fraction of damaged particles increases both with ρ^m and σ^{pm*}.

The above particle-damage map suggests three distinct regimes of crack propagation schematically represented in Fig. 9: 1) Below the particle-

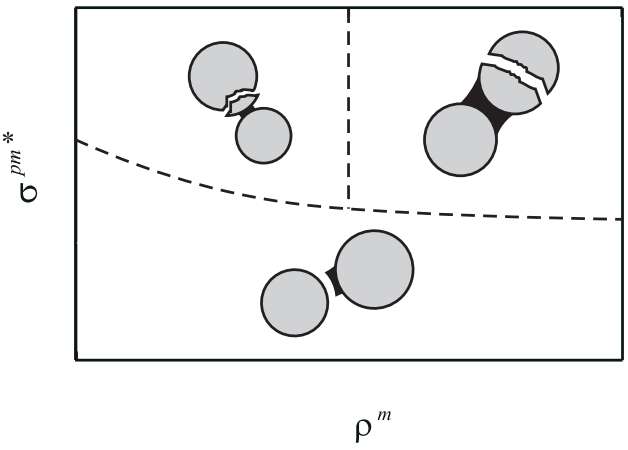

Figure 9: A schematic representation of cracking regimes as a function of matrix volume fraction ρ^m and particle-matrix effective adhesion σ^{pm*} .

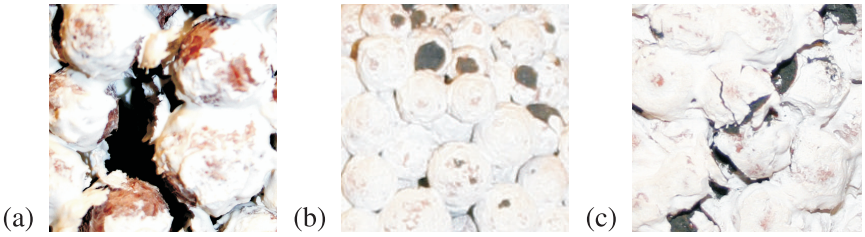

Figure 10: Examples of crack patterns corresponding to the regimes of no particle damage (a), particle abrasion (b) and particle breaking (c).

damage limit, the cracks bypass the particles and propagate through the matrix, the pores or along the particle-matrix interface; 2) Above this limit and for $\rho^m < 0.2$, the cracks penetrate also partially into the particles from solid bridges that strongly concentrate stresses and lead thus to surface abrasion of the particles; 3) Above this limit and for $\rho^m > 0.2$, the cracks propagate inside the matrix as well as across the particles, causing the breaking of the particles. Fig. 10 shows three photographs that illustrate the three cracking regimes at the particle scale. These photographs correspond to the three failure modes shown in Fig. 3.

Particle damage results from the penetration of cracks into the particles if the particles are less tough than the particle-matrix interface [13, 2, 33]. The fracture toughness $K_c = (EG_c)^{1/2}$ in traction (mode I) of a material combines the stiffness E (controlling the amount of elastic energy stored per unit volume) with the fracture energy G_c (energy required to create a crack of unit area). This expression of K_c describes a continuous medium. It

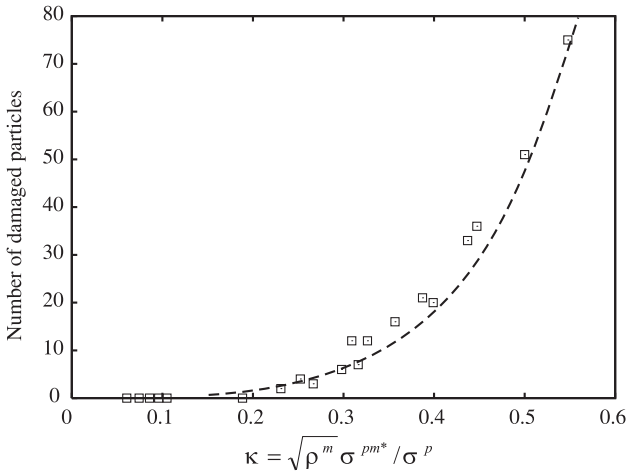

Figure 11: Number of damaged particles vs. the parameter κ (see text) for all our experimental data. The dashed line represents a quadratic fit.

can, however, be extended to granular media by replacing G_c by the contact debonding energy (energy to break a bond) and E by the elastic energy stored in the contact network.

In our system, the elastic energy is mainly localized at the interface zones between the particles due to the much higher stiffness of the particles compared to the matrix and silicone. Assuming that this energy is fully dissipated in debonding between two particles, and neglecting Poisson's ratio, the fracture energy is given by $G_c = 2eS^{pm}(\sigma^{pm*})^2/(2E)$. With the approximation $S^{pm} \propto \rho^m$, we thus expect $K_c \propto (\rho^m)^{1/2}\sigma^{pm*}$. Normalizing the latter by the tensile strength σ^p of the particles, we define the normalized parameter

$$\kappa = \frac{\sigma^{pm*}}{\sigma^p}(\rho^m)^{1/2}. \tag{8}$$

This parameter is expected to control crack propagation from the matrix to the particles.

Figure 11 shows the number of damaged particles as a function of κ for all our experimental data. It is remarkable that all data points from all tests collapse on a single plot. Below $\kappa \simeq 0.2$, no particle damage occurs. Beyond this point, the fraction of damaged particles increases nearly quadratically with κ. In this way, the parameter κ, combining σ^{pm*} and ρ^m, appears to be the control parameter both for the particle damage limit and for crack propagation through the particles.

Despite the limited number of tests, our experiments provide clear trends that highlight convincingly the respective roles of the cementing matrix and particle-matrix adherence in the mechanical behavior and failure of our model system. Further experimental work is under way in order to extend

the data points and check the effect of particle volume fraction.

4 Two-dimensional simulations

In this section, we first briefly introduce the numerical model. Then, we present our numerical results which will be discussed and compared with the experiments. It should be noted that the goal of these 2D numerical simulations is not to fit the experimental data. We are mainly interested in the influence of the matrix volume fraction and particle-matrix adhesion on the mechanical behavior.

4.1 Lattice element method

We used a lattice-based model in which different phases (particles, matrix, particle-matrix interface) are discretized as linear elastic elements forming a triangular network; see Fig. 12b for a schematic representation [25, 27, 37, 26, 19, 21, 11, 6, 4]. The stiffness of each phase is controlled by the elastic parameters of its elements whereas its fracture corresponds to the breaking of the elements at a threshold expressed in force or energy. Hence, in contrast to discrete element methods, the lattice element method (LEM) allows naturally for particle breaking and the treatment of a continuous matrix between the particles. A detailed description of the LEM and its implementation can be found in Ref. [32].

A snapshot of a 2D numerical sample is shown in Fig. 12a. The particles have the same size distribution as in experiments. The sample is built using a geometrical approach designed to generate dense granular packings for given distribution of particle diameters [38]. These samples are then compacted under isotropic compression by means of discrete element simulations. Finally, the matrix is distributed between the particles in the form of trapezoidal bonds with variable width depending on the total amount of matrix. At high levels of the matrix volume fraction ρ^m, the bonds overlap and the porosity can be reduced down to zero. The particle volume fraction $\rho^p = 0.8$ is the same for all samples. The particle-matrix adhesion is the only source of cohesion for the material. The interparticle zones are thus bare (with no matrix interposed) and can be considered as initial cracks in the sample.

All samples are subjected to axial compression with free side boundaries. Step-wise displacements are applied to nodes forming the upper boundary of the sample. The lower boundary is a line defined by nodes which are constrained to remain immobile. The initial state is the reference configuration and the equilibrium state at each step is calculated by searching the minimum of the total potential energy of the system by means of the conjugate gradient method. This "quasi-static" driving of the system leads to

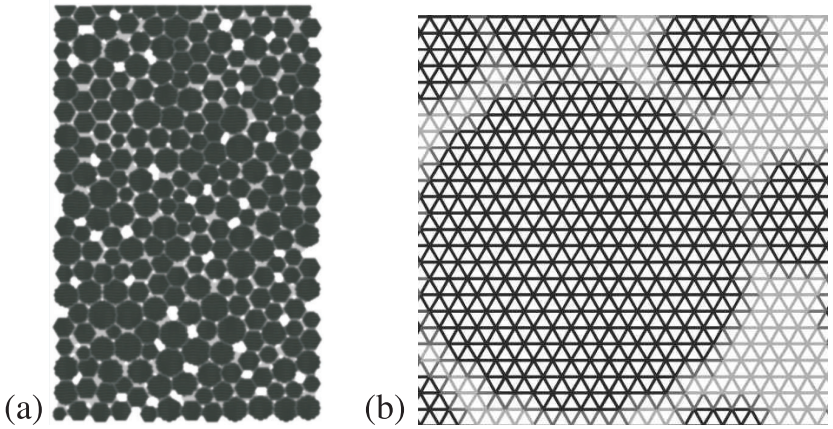

Figure 12: (a) A numerical sample composed of particles (in black), the cementing matrix (in grey) and voids (in white); (b) A zoom on the discretized particles and matrix.

irreversible rupture of overloaded elements occurring mostly in cascade. All overloaded elements are broken simultaneously within a computation step.

The local parameters of the model are the length a of the lattice vector, the spring constants k^p, k^m and k^{pm} of the elements belonging to particles, matrix and their interface, respectively, as well as the corresponding tensile force thresholds f^p, f^m and f^{pm}. Since we are interested in the *effective* compressive strength σ_Y it is dimensionally convenient to express the local thresholds in stress units. We thus define the equivalent debonding stresses $\sigma^i \equiv f^i/a$, where the exponent i refers to each phase 'p' or 'm', or the interface 'pm'. On the other hand, the equivalent stiffness of each phase or interface depends on the lattice form and spring constant. For a regular triangular lattice, we have $E^i = \alpha k^i$, where α depends on the direction of compression. We used the same values of the ratios E^p/E^m and σ^p/σ^s as in experiments. We assume that $E^{pm} = E^p E^m/(E^p + E^m)$ corresponding to a serial combination of the particle and matrix elements at the interface.

4.2 Numerical results

Figure 13 shows typical stress-strain plots for two different values of the matrix volume fraction ρ^m. In both cases, we observe a brittle behavior characterized by an effective stiffness E and strength σ_Y (peak stress). The behavior appears to be more brittle than in experiments (see Fig. 3). Let us also remark that the effective stiffness in the simulations depends only on ρ^m whereas in experiments it is controlled both by both ρ^m and ρ^s. In the simulations, the effective stiffness E increases linearly with ρ^m as shown in Fig. 14.

Figure 15 shows the compressive strength σ_Y as a function of $\rho^m \sigma^{pm}$.

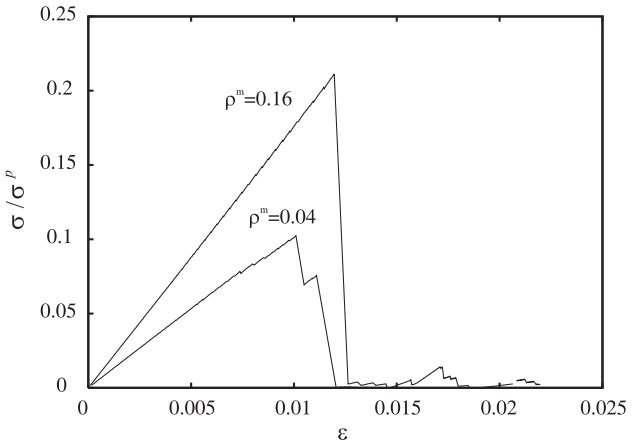

Figure 13: Axial stress normalized by the particle tensile strength as a function of axial strain for two different values of the matrix volume fraction ρ^m in lattice-element simulations.

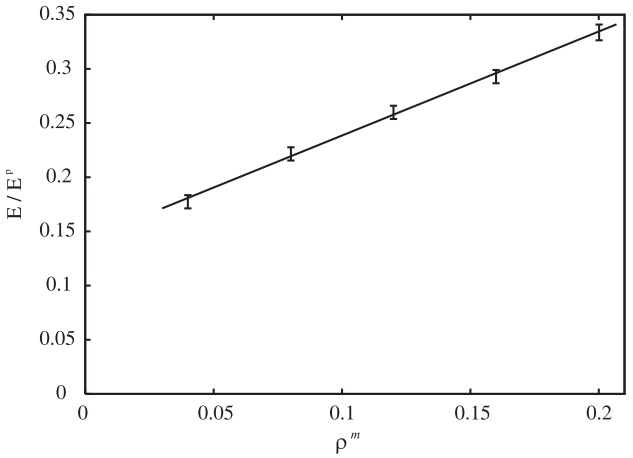

Figure 14: Effective stiffness E normalized by the particle stiffness as a function of the matrix volume fraction ρ^m.

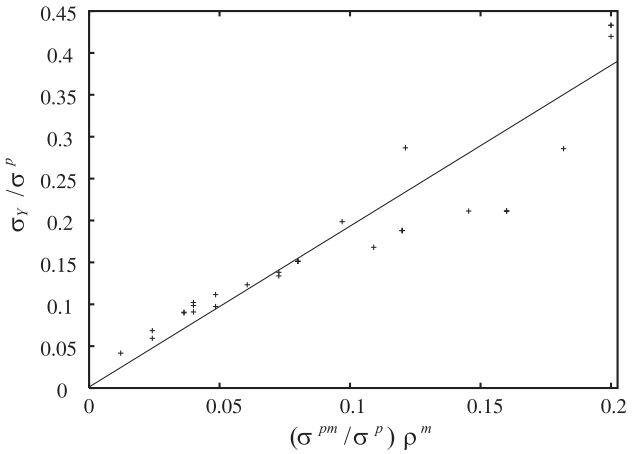

Figure 15: Compressive strength σ_Y vs. the product $\rho^m\sigma^{pm}$ from numerical data.

As in experiments (see Fig. 7), the data collapse on the same straight line passing through the origin. Deviations of data points from linear fit can be observed beyond $\rho^m\sigma^{pm} \simeq 0.1$. A similar effect can be observed in Fig. 7 for $\rho^m\sigma^{pm} \simeq 0.3$ in the experiments.

In order to characterize particle damage in the simulations, we consider the proportion n_b of broken elements in the particles with respect to the number of broken elements in the whole system. This definition does not correspond exactly to the fraction of damaged particles that we measured in the experiments. But it has the advantage of accounting for the extent of fracture inside the particles and provides richer statistics than in the experiments. Figs. 16 displays a gray-level map of n_b in the parameter space (ρ^m,σ^{pm}). It compares well to the map for the fraction of damaged particles in the experiments; see Fig. 8. In particular, we readily observe the a particle-damage limit which has the same shape as in experiments. The characteristic value of the matrix volume fraction is $\rho^m \simeq 0.1$ (to be compared with $\rho^m \simeq 0.2$ in the experiments. This is consistent with the fact that the percolation of the matrix is expected to occur at lower values in 2D (the particle volume fraction being $\simeq 0.8$) than in 3D (the particle volume fraction being $\simeq 0.58$).

We now consider the particle damage as a function of the toughness K_c in traction. In contrast to the experiments, the toughness can be evaluated at the scale of the lattice bonds. In our numerical system, the elastic energy of a particle-matrix bond at failure is $(f^{pm})^2/(2k^{pm})$, and this energy is fully dissipated when the bond fails. Hence, the adhesion energy (per unit length in 2D) is

$$G_c^{pm} = \frac{(f^{pm})^2}{2ak^{pm}}. \tag{9}$$

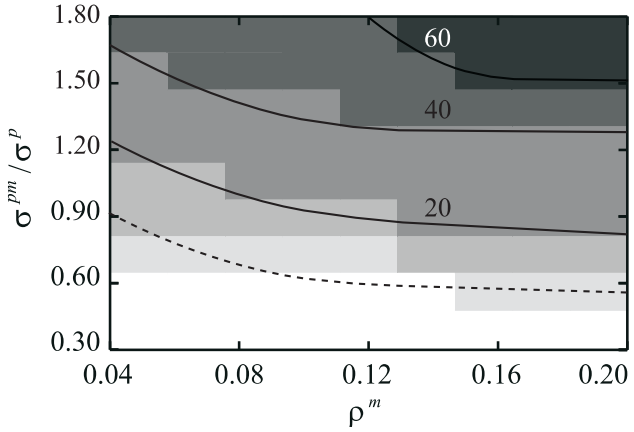

Figure 16: A grey-level map of the fraction n_b of broken bonds in numerical simulations as a function of the matrix volume fraction ρ^m and particle-matrix adhesion σ^{pm}.

Using this expression, the particle-matrix interface toughness is given by

$$K_c^{pm} = (E_{eff}^t G_c^{pm})^{\frac{1}{2}} \tag{10}$$

We normalize K_c^{pm} by the toughness K_c^p of the particles to define the "relative toughness" $K_c^r \equiv K_c^{pm}/K_c^p$. In Fig. 17 is plotted the fraction n_b of broken bonds in the particle phase as a function of K_c^r for all our simulation data. As in the experiments, below a characteristic toughness $K_c^r \simeq 0.2$, no particle damage occurs. Beyond this point, the fraction of broken bonds increases nearly linearly with K_c^r within statistical precision and saturates to 1 beyond $K_c^r \simeq 0.6$. Given the definition of n_b, this saturation means that nearly all bonds break inside the particles. This does not mean that all particles are damaged. The saturation regime corresponds to the limit where the particle-matrix adhesion is of the order of or larger than the particle tensile strength. This limit does not occur in our experiments where the total number of damaged particles are considered, and not the broken bonds.

In summary, as far as the evolution of the compressive strength and damage with particle-matrix adhesion and matrix volume fraction are considered, our numerical results are in excellent qualitative agreement with the experimental data. Both simulations and experiments reveal three regimes of particle damage controlled by a toughness parameter. Let us also mention that the simulations were also used to investigate the case of simple traction. Similar trends were found also for the effective tensile strength and particle damage [32].

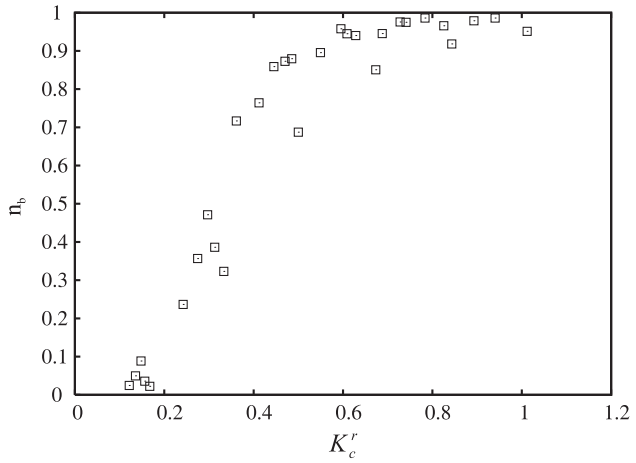

Figure 17: Fraction n_b of broken bonds in the particle phase vs relative toughness K_c^r (see text).

5 Conclusion

In this paper, we introduced an experimental model of cemented granular materials as a particular class of materials involving the characteristics of both particle-reinforced composites (due to the cementing matrix) and granular media (due to particle jamming). The samples consist of LECA beads as particles, a joint seal paste as cementing matrix and silicone coatings used to control the particle-matrix adherence. We mainly focused on the influence of matrix volume fraction and particle-matrix adhesion on the compressive strength and particle damage. We also used the lattice-element method in order to simulate 2D cemented granular samples, and the numerical data were analyzed along the same lines as in experiments.

Interestingly, for the whole investigated range of matrix volume fractions, both experiments and simulations show that the compressive strength scales with the product of matrix volume fraction and particle-matrix adhesion. On the other hand, our numerical and experimental data show that particle damage is controlled by a toughness parameter pertaining to the contact debonding energy. Below a critical value of this parameter, no particle damage occurs. Beyond this limit, particle damage increases with the toughness parameter. On the basis of particle damage data as a function of the matrix volume fraction and particle-matrix adhesion, three distinct regimes of crack propagation are identified.

This work provides for the first time direct experimental evidence for the role of matrix content and particle-matrix adherence in the cohesion of cemented granular media. However, more experiments are necessary in order to extend the range of parameters (matrix volume fraction, adhesion) and to evaluate the robustness of the results with respect to the experimental

and numerical preparation protocol. In the same way, the effect of silicone coating requires a more detailed investigation. Finally, the numerical approach by the lattice element method proves to be a promising tool, but it needs to be extended to three dimensions for a direct comparison with the experiments.

acknowledgements

We acknowledge technical help by A. Clary and G. Camp.

References

[1] A. Benhamida, F. Bouchelaghem, and H. Dumontet. Effective properties of a cemented or an injected granular material. *International Journal for Numerical and Analytical Methods in Geomechanics*, 29:187–208, February 2005.

[2] Oral Buyukozturk and Brian Hearing. Crack propagation in concrete composites influenced by interface fracture parameters. *International Journal of Solids and Structures*, 35(31-32):4055–4066, November 1998.

[3] A. Castellanos. The relationship between attractive interparticle forces and bulk behaviour in dry and uncharged fine powders. *Advances In Physics*, 54:263–376(114), Number 4/June 2005.

[4] B. M. Chiaia, A. Vervuurt, and J. G. M. Van Mier. Lattice model evaluation of progressive failure in disordered particle composites. *Engineering Fracture Mechanics*, 57(2-3):301–309, 1997.

[5] F. de Larrard and A. Belloc. The influence of aggregate on the compressive strength of normal and high-strength concrete. *ACI materials journal*, 94:417–426, 1997.

[6] Arnaud Delaplace, Gilles Pijaudier-Cabot, and Stephane Roux. Progressive damage in discrete models and consequences on continuum modelling. *Journal of the Mechanics and Physics of Solids*, 44(1):99–136, January 1996.

[7] Jean-Yves Delenne, Moulay Saïd El Youssoufi, Fabien Cherblanc, and Jean-Claude Benet. Mechanical behaviour and failure of cohesive granular materials. *International Journal for Numerical and Analytical Methods in Geomechanics*, 28(15):1577–1594, 2004.

[8] J.Y. Delenne, Y. Haddad, J.C. Benet, and J. Abecassis. Use of mechanics of cohesive granular media for analysis of hardness and vitreousness

of wheat endosperm. *Journal of Cereal Science*, 47(3):438–444, May 2008.

[9] M. S. El Youssoufi, J.-Y. Delenne, and F. Radjaï. Self-stresses and crack formation by particle swelling in cohesive granular media. *Phys. Rev. E*, 71:051307, 2005.

[10] David Elata and Jack Dvorkin. Pressure sensitivity of cemented granular materials. *Mechanics of Materials*, 23(2):147–154, June 1996.

[11] J. Fitoussi, G. Guo, and D. Baptiste. A statistical micromechanical model of anisotropic damage for s.m.c. composites. *Composites Science and Technology*, 58(5):759–763, 1998.

[12] J. D. Goddard. Microstructural origins of continuum stress fields - a brief history and some unresolved issues. In D. DeKee and P. N. Kaloni, editors, *Recent Developments in Structured Continua. Pitman Research Notes in Mathematics No. 143*, page 179, New York, 1986. Longman, J. Wiley.

[13] Ming-Yuan He and John W. Hutchinson. Crack deflection at an interface between dissimilar elastic materials. *International Journal of Solids and Structures*, 25(9):1053–1067, 1989.

[14] H. J. Herrmann and S. Roux, editors. *Statistical Models for Fracture in Disordered Media*. North Holland, Amsterdam, 1990.

[15] K.L. Johnson. *Contact Mechanics*. University Press, Cambridge, 1999.

[16] K. Kendall, N.McN. Alford, and J.D. Birchall. The strength of green bodies. *British Ceramic Proceedings*, 37:255–265, 1986.

[17] Andrea J. Liu and Sidney R. Nagel, editors. *Jamming And Rheology*. Taylor and Francis, New York, 2001.

[18] I. J. Merchant, D. E. Macphee, H. W. Chandler, and R. J. Henderson. Toughening cement-based materials through the control of interfacial bonding. *Cement and Concrete Research*, 31(12):1873–1880, December 2001.

[19] L. Mishnaevsky, Jr., K. Derrien, and D. Baptiste. Effect of microstructure of particle reinforced composites on the damage evolution: probabilistic and numerical analysis. *Composites Science and Technology*, 64(12):1805–1818, September 2004.

[20] C.F. Morris. Puroindolines: the molecular genetic basis of wheat grain hardness. *Plant Molecular Biology*, 48:633–647, 2002.

[21] Carole Nadot-Martin, Herve Trumel, and Andre Dragon. Morphology-based homogenization for viscoelastic particulate composites: Part i: Viscoelasticity sole. *European Journal of Mechanics - A/Solids*, 22(1):89–106, 2003.

[22] H. Ouadfel and L. Rothenburg. Stress-force-fabric relationship for assemblies of ellipsoids. *Mechanics of Materials*, 33(4):201–221, 2001.

[23] F. Radjaï, I. Preechawuttipong, and R. Peyroux. Cohesive granular texture. In P. A. Vermeer, S. Diebels, W. Ehlers, H. J. Herrmann, S. Luding, and E. Ramm, editors, *Continuous and discontinuous modelling of cohesive frictional materials*, 2000.

[24] Vincent Richefeu, Moulay Said El Youssoufi, and Farhang Radjai. Shear strength properties of wet granular materials. *Physical Review E (Statistical, Nonlinear, and Soft Matter Physics)*, 73(5):051304, 2006.

[25] S. Roux. *Statistical Models for Fracture in Disordered Media*, chapter Continuum and discrete description of elasticity and other rheological behavior, pages 87–114. North Holland, Amsterdam, 1990.

[26] M. Sahimi. *Heterogeneous Materials II.* Springer, New York, 2003.

[27] E. Schlangen and J. G. M. van Mier. Experimental and numerical analysis of micromechanisms of fracture of cement-based composites. *Cement and Concrete Composites*, 14(2):105–118, 1992.

[28] F. Sienkiewicz, A. Shukla, M. Sadd, Z. Zhang, and J. Dvorkin. A combined experimental and numerical scheme for the determination of contact loads between cemented particles. *Mechanics of Materials*, 22(1):43–50, January 1996.

[29] H. Tan, Y. Huang, C. Liu, and P.H. Geubelle. The mori-tanaka method for composite materials with nonlinear interface debonding. *International Journal of Plasticity*, 21(10):1890–1918, October 2005.

[30] H. Tan, Y. Huang, C. Liu, G. Ravichandran, H.M. Inglis, and P.H. Geubelle. The uniaxial tension of particulate composite materials with nonlinear interface debonding. *International Journal of Solids and Structures*, 44(6):1809–1822, March 2007.

[31] Edward J. Tarbuck and Frederic K. Lutgens. *Earth – An introduction to Physical Geology.* Pearson Education, New Jersey, 2005.

[32] V. Topin, J.-Y. Delenne, F. Radjai, L. Brendel, and F. Mabille. Strength and fracture of cemented granular matter. *The European Physical Journal E*, 23:413–429, 2007.

[33] Vincent Topin, Farhang Radjai, Jean-Yves Delenne, and Frédéric Mabille. Mechanical modeling of wheat hardness and fragmentation. *Powder Technology*, In Press, Corrected Proof:–, 2008.

[34] Vincent Topin, Farhang Radjai, Jean-Yves Delenne, Abdelkrim Sadoudi, and Frédéric Mabille. Wheat endosperm as a cohesive granular material. *Journal of Cereal Science*, 47(2):347–356, March 2008.

[35] H. Troadec, F. Radjai, S. Roux, and J.C. Charmet. Model for granular texture with steric exclusion. *Physical Review E*, 66(4 1):041305–1, 2002.

[36] K. M. Turnbull and S. Rahman. Endosperm texture in wheat. *Journal of Cereal Science*, 36(3):327–337, November 2002.

[37] J. G. M. Van Mier, B. M. Chiaia, and Adri Vervuurt. Numerical simulation of chaotic and self-organizing damage in brittle disordered materials. *Computer Methods in Applied Mechanics and Engineering*, 142(1-2):189–201, March 1997.

[38] C. Voivret, F. Radjai, J.-Y. Delenne, and M. S. El Youssoufi. Space-filling properties of polydisperse granular media. *Phys. Rev. E*, 76(2):021301–12, August 2007.

[39] Li Zhonghua and S. Schmauder. Phase-stress partition and residual stress in metal matrix composites. *Computational Materials Science*, 18(3-4):295–302, September 2000.

[40] C. W. Zhou, W. Yang, and D. N. Fang. Mesofracture of metal matrix composites reinforced by particles of large volume fraction. *Theoretical and Applied Fracture Mechanics*, 41(1-3):311–326, April 2004.